# Direct Numerical Simulations of Shock-Boundary Layer Interaction at $Ma = 6$ *

Alessandro Pagella

Ulrich Rist

*Universität Stuttgart, Institut für Aerodynamik und Gasdynamik, Pfaffenwaldring 21, 70550 Stuttgart, Germany*

July 9, 2003

Two boundary layers with impinging shock wave at $Ma = 6$, $T_\infty = 78K$ and a shock angle with respect to the wall of $\sigma = 12^o$ are compared: a boundary layer with insulated wall and a cooled case with $T_w = 300K$. As expected, the length of the separation bubble is smaller for the case with cooled wall. Linear stability calculations show, that the first instability mode could be completely stabilised by wall cooling in the underlying case. However, it is known that cooling destabilizes higher, acoustic modes, which is the case here, too. An oblique breakdown scenario reveals the formation of longitudinal vortices in both cases with shock, mainly promoted by the non-linear growth of the $(0, 2)$ mode. The maximum disturbance amplitudes are larger for the case with insulated wall and the disturbance parameters chosen. The structure of the $(0, 2)$ mode is different in the cases with shock, compared to the boundary layer without shock. The wall-normal velocity component $v$ in the base flow of the boundary layer without shock counteracts the formation of longitudinal vortices in the total flow.

## 1. Introduction

In practice, hypersonic flow-situations mainly occur during re-entry into the earth atmosphere. Re-entry is one of the most critical situations during a space-flight mission. A failure of structure is difficult to handle, possibly leading to a total loss of the vessel. Therefore, a profound knowledge of the physics is absolutely necessary. Hypersonic flow is defined at Mach numbers of four to five and higher. There are three main physical effects to be considered:

*Real gas effects.* During the re-entry trajectory at a certain flight level a space vessel encounters very high temperatures, which do not allow to consider an ideal gas within this particular flow regime. If such high-temperature flows are intended to be investigated, real gas behaviour has to be modelled and can not be neglected. In the underlying work, these real gas effects are not taken into account. We limit ourselves to cold flows below $\approx 2500K$, the borderline to dissociation at standard conditions, with a smaller Mach-number at the lower end of the hypersonic regime. At this flow conditions, a real-gas assumption is justified. Taking real gas effects into account certainly is subject to further studies.

*Project funded by *Deutsche Forschungsgemeinschaft* within *Sonderforschungsbereich 259*. Computer time provided by the High Performance Computing Centre in Stuttgart (*HLRS*).

*Shock bounday layer interaction.* In flows faster than the speed of sound, a change in direction always results in either a compression or expansion, depending on the direction of the turnaround. Compression waves can merge into a shock, which in turn is very likely to hit a boundary layer on the structure of the craft. In fact this so-called shock-boundary layer interaction is a major source of high heat or pressure loads and often causes separation of the flow. In hypersonic flows, these loads can become very high. Shock-boundary layer interactions were studied from the mid 1940's. First systematic experimental studies have been carried out by Ackeret et al. [2] and Liepmann [18]. Due to the pressure rise, an impinging shock-wave causes the boundary layer to thicken. It penetrates into the boundary layer ending at the sonic line as an almost vertical shock. There it is reflected as a system of expansion waves. Provided the pressure gradient is strong enough, the boundary layer separates. The thickening results in a deflection of the flow yielding compression waves near separation and reattachment. Well outside the boundary layer, they coalesce to the separation and reattachment shock, respectively. A more thorough description of shock-boundary layer interactions can be found in [7].

*Transition to turbulence.* Transition from a laminar to a turbulent flow comprises high aerodynamic loads, as well. It has been a major area of concern in the past decades and a lot of research has been carried out on the aspects of understanding and possibly influencing transition. However, although a lot of progress has been achieved the physics are far from being understood. For compressible flows, such as hypersonic flows, much less has been done compared to incompressible flows. For the first phase of the transition process, quantitative predictions can be made with compressible linear stability theory, which was formulated by Mack [19]. Eißler & Bestek [8] and Fezer & Kloker [11] investigated transition to turbulence of flat-plate boundary layers at Mach numbers ranging from about four to six. Experiments with controlled, artificial disturbances in hypersonic flows are very difficult to perform. Therefore, only few are known [16], [10].

## 2. Numerical Scheme

**Governing Equations** The numerical scheme is based on the complete, three-dimensional, unsteady, compressible Navier-Stokes equations for Cartesian coordinates in conservative formulation:

$$\frac{\partial \rho}{\partial t} + \nabla \cdot (\rho \mathbf{u}) = 0 \tag{1}$$

$$\frac{\partial (\rho \mathbf{u})}{\partial t} + \nabla \cdot (\rho \mathbf{u}\mathbf{u}) + \nabla p = \frac{1}{Re} \nabla \cdot \sigma \tag{2}$$

$$\frac{\partial (\rho e)}{\partial t} + \nabla \cdot (p + \rho e)\mathbf{u} = \frac{1}{(\kappa - 1) Re\, Pr\, Ma^2} \nabla \cdot (\vartheta \nabla T) + \frac{1}{Re} \nabla \cdot (\sigma \mathbf{u}) \,, \tag{3}$$

where

$$\sigma = \mu \left[ (\nabla \mathbf{u} + \nabla \mathbf{u}^T) - \frac{2}{3} (\nabla \cdot \mathbf{u}) \mathbf{I} \right] \tag{4}$$

with the velocity vector $\mathbf{u} = [u, v, w]^T$.
The energy is calculated as

$$e = \int c_v \, dT + \frac{1}{2}(u^2 + v^2 + w^2). \tag{5}$$

The fluid is a non-reacting, ideal gas with constant Prandtl number $Pr = 0.71$ and specific heat ratio $\kappa = c_p/c_v = 1.4$, with $c_p$ and $c_v$ as the specific heat coefficients at constant pressure and volume, respectively. Viscosity $\mu$ for temperatures above the Sutherland temperature $T_s$ is calculated by Sutherland's law, for temperatures below $T_s$ with the relation $\mu/\mu_\infty = T/T_\infty$. The thermal conductivity coefficient $\vartheta$ is proportional to the viscosity. In our simulations, all lengths are made non-dimensional with a reference length $L$, which appears in the global Reynolds number $Re = \rho_\infty \cdot u_\infty \cdot L/\mu_\infty = 10^5$. A local Reynolds number is defined as $R_x = \sqrt{x \cdot Re}$. The specific heat $c_v$ is normalised with $u_\infty^2/T_\infty$ (with $T_\infty$ giving the free-stream temperature) and time $t$ is normalised with $L/u_\infty$, where $u_\infty$ is the free-stream velocity. Density $\rho$, temperature $T$ and viscosity $\mu$ are standardised by their respective free-stream values.

Figure 1 shows the integration domain. The calculation starts at $X_0$, the end of the integration domain is given by $X_N$. $X_s$ gives the location of the shock, which is prescribed at the free-stream boundary. A buffer domain [14] can be switched on at $X_3$ damping the disturbances in order to provide an undisturbed, laminar flow at the outflow boundary. The disturbance strip is located between $X_1 \leq x \leq X_2$. The disturbances are periodic in spanwise direction, having a wavelength of $\lambda_z$ and determining the width of the integration domain as $z_N = \lambda_z$.

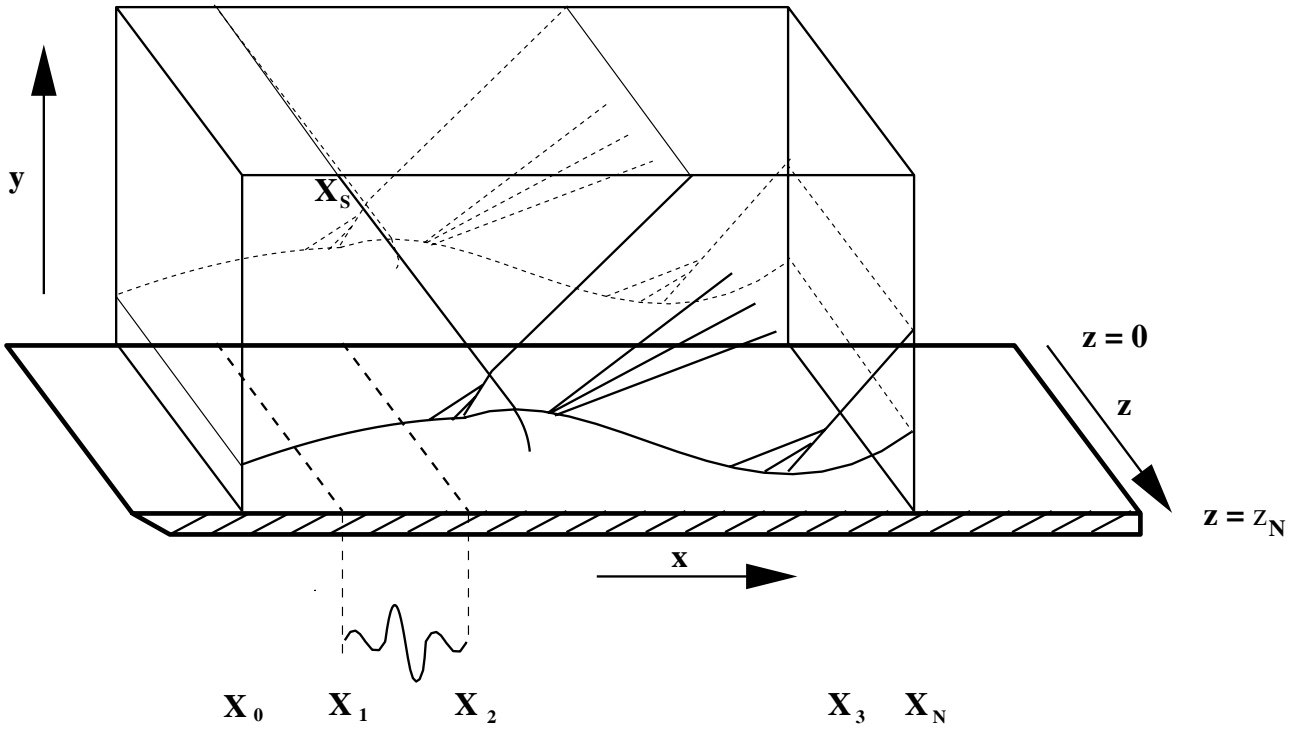


Figure 1. Integration domain.

**Discretisation** For a more thorough description of the numerical scheme the reader is referred to [23] and [9]. Time integration is performed at equidistant time steps with a standard Runge-Kutta scheme of fourth-order accuracy (see for example [13]). In streamwise direction, compact

finite differences of sixth-order accuracy are applied, which are in a split-type formulation in order to have some damping properties with regard to small-scale numerical oscillations ([15]), which occur at the high gradients resulting from the shock. In the split-type formulation, the weighting of the numerical stencil alternates each Runge-Kutta step from downwind to upwind and vice versa. Near the boundaries, differences of fourth and second order of magnitude are applied ensuring the stencils remain within the integration domain. If a stronger shock is present, the damping characteristic of the split-type formulation is not sufficient enough *in the two-dimensional base-flow calculation*. In this case, an implicit filter of fourth-order accuracy ([17]) is applied to filter the variables of the solution vector each physical time step in streamwise direction:

$$\alpha\hat{f}_{i-1} + \hat{f}_i + \alpha\hat{f}_{i+1} = af_i + \frac{c}{2}(f_{i+2} + f_{i-2}) + \frac{b}{2}(f_{i+1} + f_{i-1})\,, \tag{6}$$

with

$$a = \frac{1}{8}(5 + 6\alpha), \quad b = \frac{1}{2}(1 + 2\alpha), \quad c = -\frac{1}{8}(1 - 2\alpha). \tag{7}$$

$\alpha$ is the filtering parameter. $\alpha = 0.5$ would mean no filtering, while $\alpha = 0.495$ is typically used in our simulations. Aware of the possible influence of the filter on the calculations, particular focus has been taken to the grid-independency of our simulations. It turned out, that with sufficiently small step-sizes no influence of the filter could be observed. Both for the filtering and the streamwise derivatives, the resulting tri-diagonal system of equations is solved by a Thomas algorithm (see e.g. [3]).

In wall-normal direction split-type finite differences of fourth-order accuracy are used to calculate convective terms, while viscous terms are calculated by fourth-order central differences. As for the streamwise derivatives, the finite differences at the boundaries are adapted to fit in the integration domain, while keeping the formal order of accuracy here.

In spanwise direction we have periodic boundaries, which allow to apply a spectral approximation with Fourier expansion (see e.g. [5]). Transformation to Fourier and physical space is performed with a standard fast-Fourier transform, such as described in [21].

**Boundary Conditions** At the free-stream boundary, a characteristic boundary condition ([12]), where the flow variables are held constant along the characteristic

$$\left(\frac{\partial y}{\partial x}\right)_+ = \tan\left(\sin^{-1}\frac{1}{Ma} + \tan^{-1}\frac{v}{u}\right) \tag{8}$$

and, more recently, a non-reflecting boundary condition, according to Thompson [22] is applied. The basic idea in this non-reflecting boundary condition is to neglect parabolic terms in the wall-normal derivatives of the Navier-Stokes equations thus obtaining a hyperbolic problem, which has to be converted into characteristic formulation. Then, incoming characteristics are set to zero.

The shock wave is introduced by holding the flow-variables constant in a limited area at the free-stream boundary, according to the Rankine-Hugoniot relations after the shock and the initial free-stream conditions before the shock.

The flow quantities at the inflow boundary result from the solutions of the compressible boundary layer equations and are held constant throughout the simulation. At the wall, a no-slip condition and vanishing normal velocities are assumed.

Disturbances are introduced at a disturbance strip located between $X_1$ and $X_2$ in figure 1 with simulated blowing and suction. The disturbance function is

$$f_{\rho v}(\varsigma, z, t) = \hat{a} * \sin(Ft) * \cos(k\beta z) * f_r(\varsigma). \tag{9}$$

In our modal discretization in spanwise direction, $k$ indicates the spanwise Fourier modes, with $k = 0$ meaning a two-dimensional disturbance. The disturbance frequency $F$ determines the streamwise wave number $\alpha_r$ via the dispersion relation of the disturbances. The spanwise wave number is $\beta$. Thus, the obliqueness angle $\psi$ is given by $tan\,\psi = (k\beta)/\alpha_r$. $\hat{a}$ is the disturbance amplitude and $f_r(\varsigma)$ the spatial disturbance function

$$f_r(\varsigma) = \varsigma^3(3\varsigma^2 - 7\varsigma + 4), \quad 0 \le \varsigma \le 1 \tag{10}$$

$$f_r(2 - \varsigma) = -f_{\rho v}(\varsigma)\,, \tag{11}$$

with

$$\varsigma = \frac{2(x - x_1)}{x_2 - x_1}. \tag{12}$$

The wall temperature can be chosen to remain either constant or adiabatic. At the outflow boundary, second derivatives are neglected. To provide an undisturbed base flow at the outflow boundary, disturbances are damped artificially [9] at a disturbance strip, located between $X_3$ and $X_N$ in figure 1.

# 3. Computational Performance

The code usually runs on the NEC SX-4 and NEC SX-5 of the High Performance Computing Centre in Stuttgart (HLRS). The results presented within this paper represent problems of small size and were therefore computed on the smaller machine, the NEC SX-4. The grid size of the base flow is $m \times n = 301 \times 1201 = 361502$, the simulations with controlled disturbances consist of a grid with $m \times n = 301 \times 650 = 195650$ grid points and $k = 10$ harmonics in spanwise direction. $m$ represents the number of grid-points in wall-normal direction, while $n$ is the number of grid points in streamwise direction. Simulations at $Ma = 6$, $\sigma = 12^o$ with insulated wall typically perform with three processors at 2688 MFLOPS using 751 MByte. Code-vectorisation is 98.8%

# 4. Results

In the following, results at $Ma = 6$ with a free stream temperature of $T_\infty = 78K$ and a shock angle of $\sigma = 12^o$ will be presented. Both simulations with adiabatic and cooled wall conditions ($T_w = 300K = const.$) have been carried out.

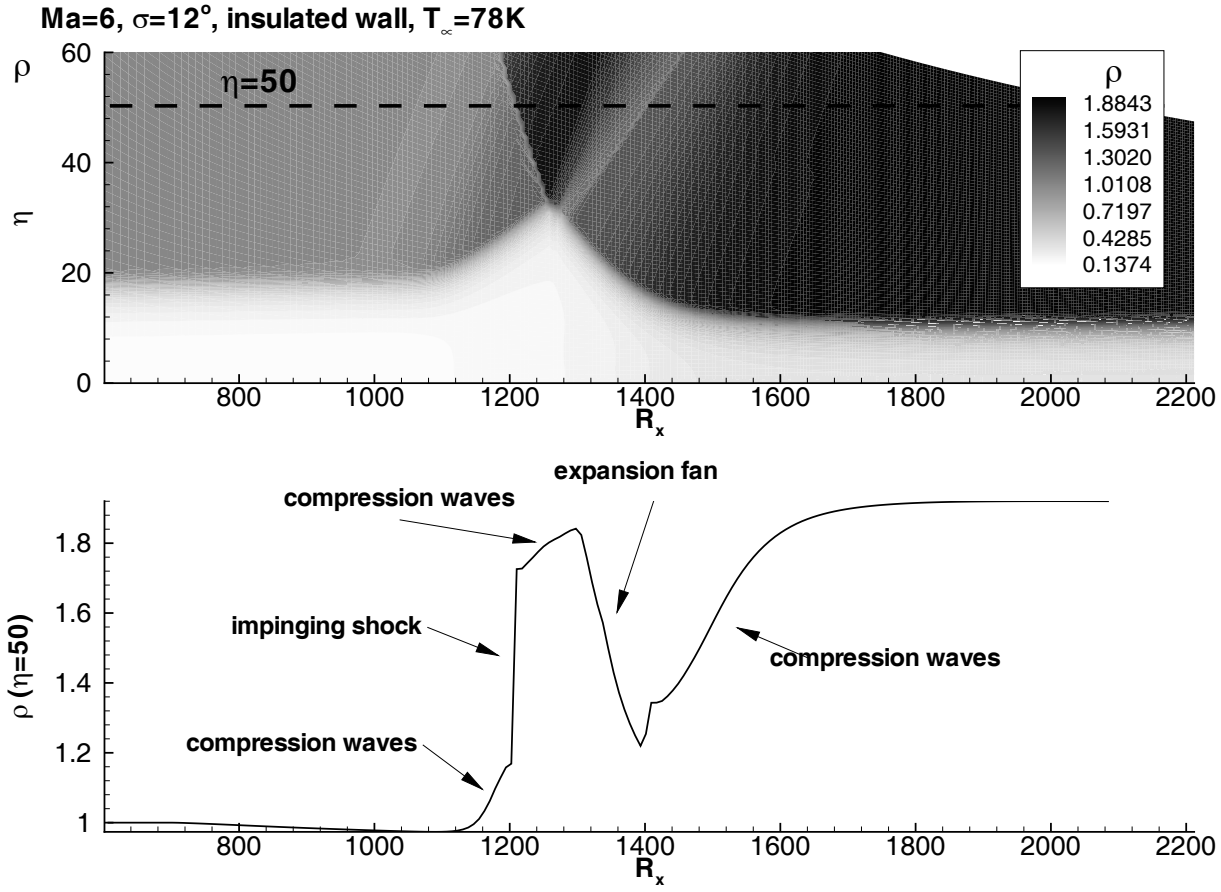


Figure 2. Density field (upper picture) and density distribution for $\eta = 50 = const.$ $Ma = 6$, $\sigma = 12^o$, insulated wall.

**Base Flow Properties** The upper picture in figure 2 gives the density field of a simulation with insulated wall and the free-stream conditions mentioned before. $\eta = y \cdot Re/R_x$ is a wall-normal similarity parameter. The thickening of the boundary layer due to the impinging shock wave can clearly be seen. It begins at $R_x \approx 1140$. Also, the boundary layer is fairly thinner behind the interaction region compared to the boundary layer upstream. The lower picture in figure 2 shows the density distribution versus $R_x$, which was extracted at $\eta = 50 = const.$ The location of typical interaction phenomena in the free stream, such as compression waves near separation and reattachment, the impinging shock wave and the expansion fan, which where already discussed in the introduction are marked accordingly.

Caused by the pressure gradient of the impinging shock wave, the boundary layer separates, provided the shock is strong enough. Figure 3 gives the skin friction distribution of both the insulated wall-case and the case with $T_w = 300K = const.$ For validation purposes, results of grid-refinement studies are also given, represented by the filled symbols. They show the grid-independency of our simulations. Simulations with both higher and longer integration domains indicated no influence of the boundaries (not shown here). The boundary layer of the cooled wall is thinner than the adiabatic boundary layer, therefore the skin friction coefficient in figure 3 of the incoming flow is larger compared to the adiabatic boundary layer. For the same shock angle of $\sigma = 12^o$, the length of the separation bubble, which can be identified by its negative skin friction, for the case with cooled wall is only $\approx 60\%$ of the length for the case

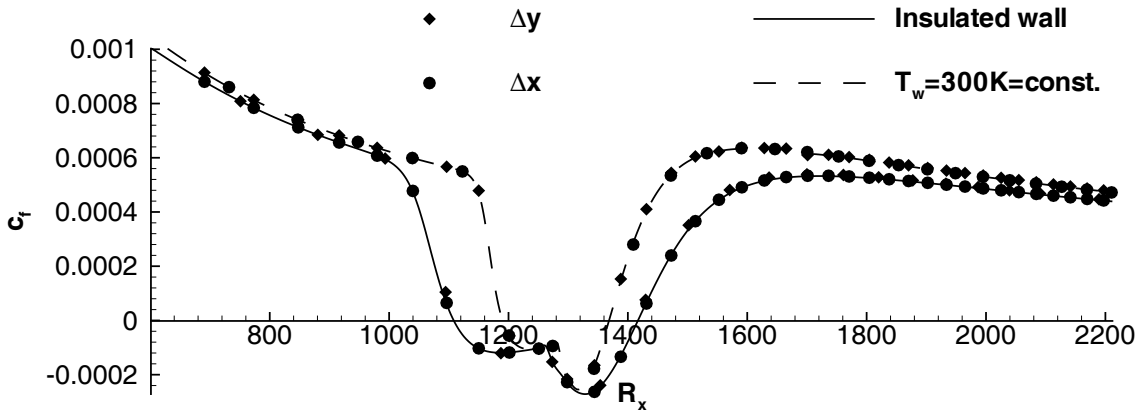


Figure 3. Skin friction distribution of both the cases with insulated wall and constant wall temperature $T_w = 300K$.

with insulated wall.

The wall-temperature distribution of the adiabatic case is given in the upper picture of figure 4. Caused by the influence of the shock, the wall temperature rises. Inside the separation bubble, the wall temperature nearly remains constant, similar to the typical plateau in the wall-pressure distribution. The total rise of the temperature over the interaction region does not exceed $13K$. The wall pressure distribution is shown in the lower picture of figure 4. The larger separation bubble of the case with insulated wall is reflected in the wall pressure distribution as well. Because the shock is not very strong, the plateau is not pronounced in both the cases with adiabatic and cooled wall. The total rise of the wall pressure over the interaction region is slightly larger for the case with constant, cooled wall-temperature.

**Small-Disturbances Development** In this section, results of compressible linear stability theory computations will be shown, which are based on the scheme developed by [19]. Figure 5 shows such computations for $Ma = 6$ without impinging shock and cooled wall (upper picture) as well as insulated wall (lower picture). Given are amplification rates $-\alpha_i = \partial ln(A(x)/A_0)/\partial x$, where $A(x)/A_0$ is the amplitude ratio of any flow variable with respect to its initial amplitude. $F$ is the disturbance frequency and $R_x$ the square root of the local Reynolds number. The solid lines in the plots, labeled with "0" are the lines of neutral amplification, darker shadings indicate larger amplification rates. In the upper part of figure 5, the case with the constant wall temperature of $T_w = 300K$, only the second instability mode is present. Wall-cooling results in a complete stabilisation of the first instability mode here. In the lower part of figure 5, the adiabatic case, both the first and second instability modes are amplified. However, the first and second modes have no distinct, separated location. They are affiliated to each other. Because of the fact, that the second mode is stronger amplified than the first mode in this configuration, the two modes still can be identified. Compared to the second mode in the case with $T_w = 300K$, the second mode of the adiabatic case has smaller amplification rates. This is an effect of wall-cooling in the case with $T_w = 300K$, too: although it stabilises the first mode, higher modes are known to be destabilised with cooling.

We now turn to the case with impinging shock wave as presented in the previous section. In figure 6 amplification rates with respect to the disturbance frequency $F$ and the square root of the local Reynolds number $R_x$ for two-dimensional linear disturbances are given. They

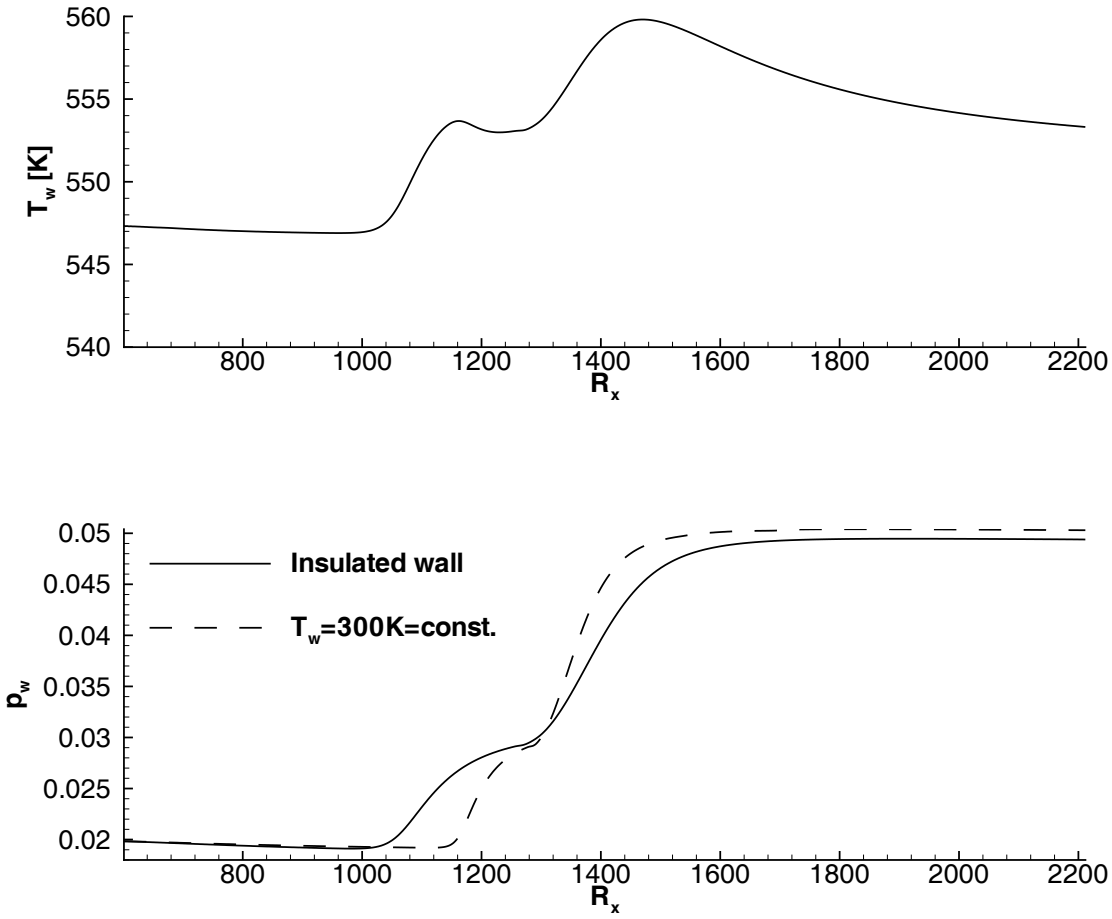


Figure 4. Wall temperature distribution of the adiabatic boundary layer (upper picture) and wall pressure distributions.

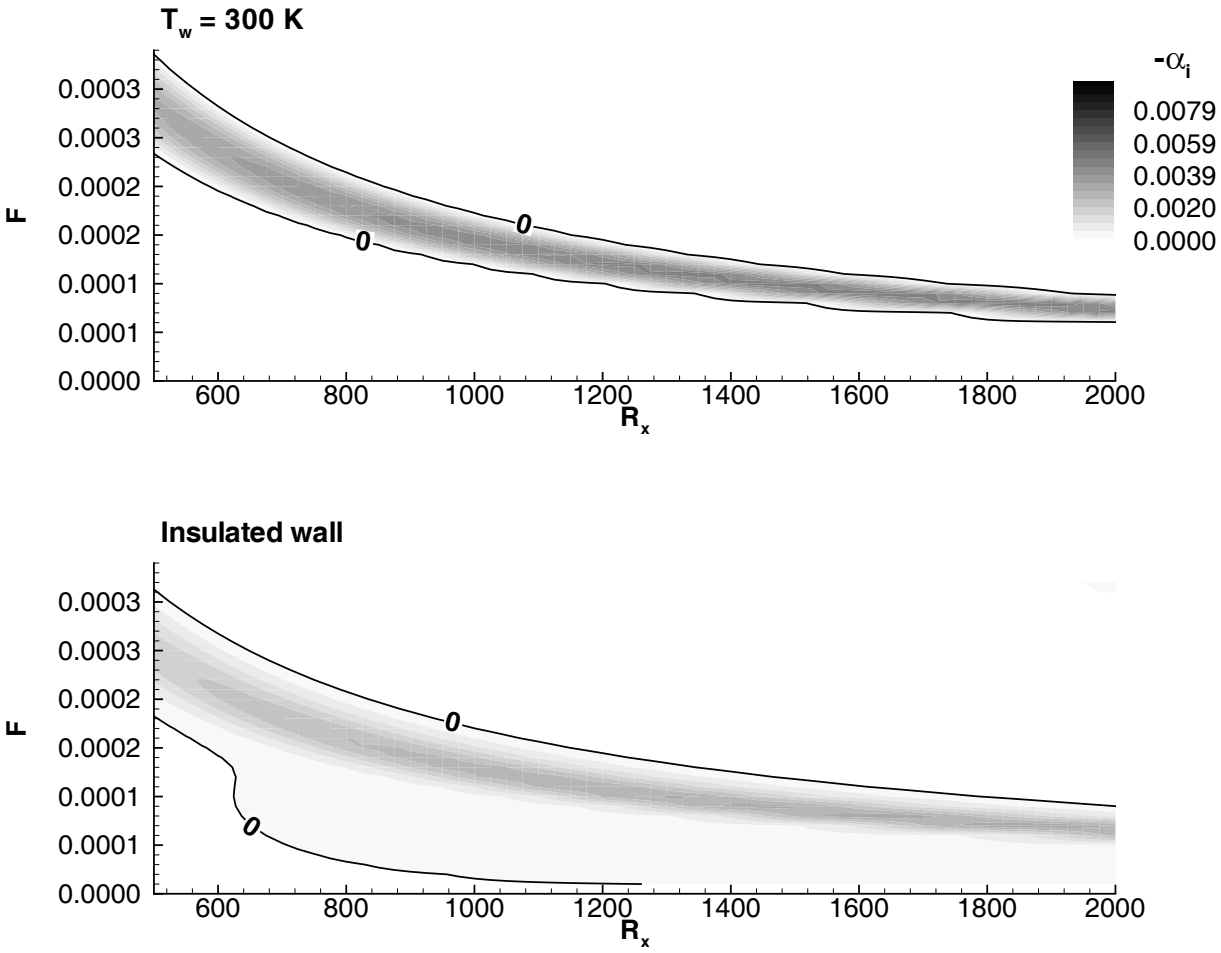


Figure 5. Amplification rates $\alpha_i$ with respect to the disturbance frequency $F$ and the square root of the local Reynolds number $R_x$. Constant wall temperature $T_w = 300K$ (upper picture) and insulated wall (lower picture). No shock.

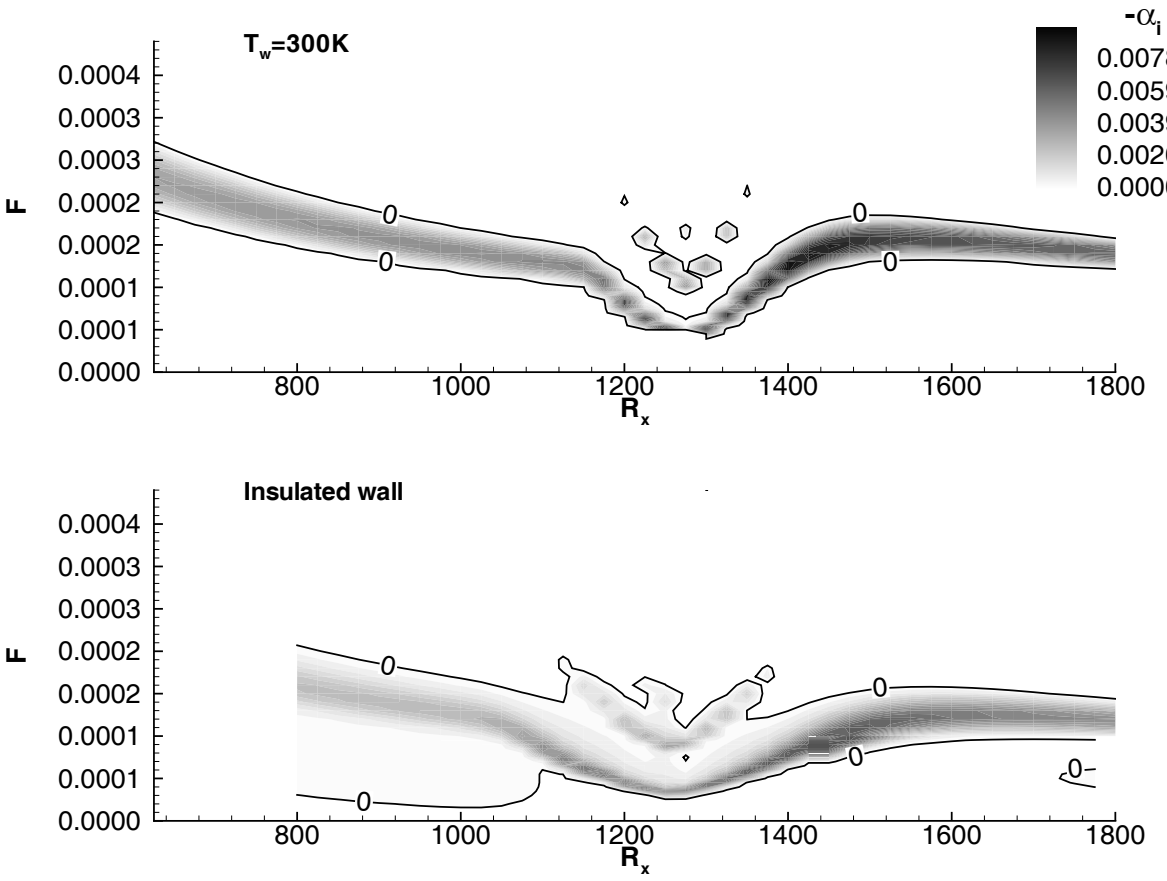


Figure 6. Amplification rates $\alpha_i$ with respect to the disturbance frequency $F$ and the square root of the local Reynolds number $R_x$. Constant wall temperature $T_w = 300K$ (upper picture) and insulated wall (lower picture). Shock angle $\sigma = 12^o$.

are obtained by extracting local $u$ and $T$ profiles from the two-dimensional direct numerical simulation presented before, which are used as input data for the linear stability solver. The upper picture in figure 6 gives the amplification rates for the case with $T_w = 300K$, while in the lower picture amplification rates for the insulated wall-case are given. The insulated wall-case behaves similar to results obtained earlier for $Ma = 4.8$, which can be found in [20]. The first mode vanishes near shock-impingement, while the second mode is increased in its amplification rate and shifted to lower frequencies. New instabilities form at higher frequencies. In [20], the increase of the second-mode amplification rates is explained by an increase of the thickness of the local supersonic flow region. Diminishing viscosity caused by the separation of the boundary layer seems to play an important role, too. The cooled-wall case, which is given in the upper picture of figure 6 shows according behaviour for its second mode instability. However, compared to the adiabatic case the amplification rates remain larger over the whole parameter range given in the plot.

The mode-identity is determined by the zeros of the pressure eigenfunction (cf. [19]). Figure 7 gives eigenfunctions and phase distributions at two different Reynolds numbers and various disturbance frequencies for the insulated case with shock. The solid lines at $R_x = 900$ correspond to a first-mode instability, because no zero is present in the eigenfunction, while the dashed line refers to a second mode (one zero). At $R_x = 900$ the boundary layer is not

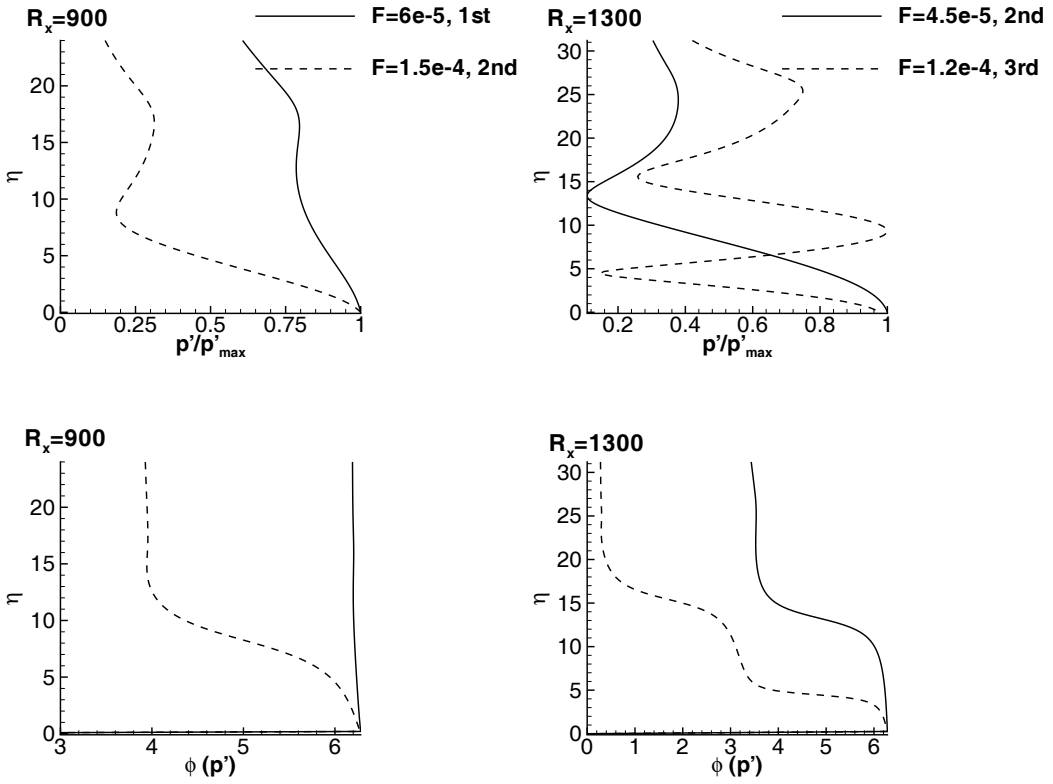


Figure 7. Pressure eigenfunctions and their corresponding phase distributions at $R_x = 900$ and $R_x = 1300$ for the adiabatic case. Shock angle $\sigma = 12^o$.

influenced by the shock-boundary layer interaction. $R_x = 1300$ lies well inside the separation bubble. The solid line in the corresponding pictures represents the eigenfunction and the phase distribution for a second mode (one zero). As briefly explained before, due to the influence of the shock, new instabilities at higher frequencies are formed near the interaction zone. Those refer to a third mode, which can be concluded from the two zeros (dashed lines in figure 7 at $R_x = 1300$).

**Larger-Disturbances Development** We now discuss the non-linear behaviour of the same configurations used in earlier sections. For $Ma = 4.5$, results for fundamental, subharmonic and oblique disturbance scenarios were shown in [1]. It turned out, that independent from the disturbance scenario a strong increase of the so-called streak or vortex modes $(0, k)$ could be observed downstream shock impingement. However, the amplitude was too small, so vortices could not be observed in the total flow. In the literature the occurrence of such vortices is typically explained with a Görtler mechanism, triggered by the concave curvature near reattachment ([4, 6]). Figure 8 shows maximum temperature amplitudes of the direct numerical simulation in the oblique case scenario, which were obtained by a timewise Fourier analysis over one disturbance period. For comparison, results of the case without impinging shock wave are given as well, represented by the solid lines with the filled circle symbols. The wall-condition is adiabatic here. In the oblique disturbance scenario, we have a single three-dimensional disturbance wave, of which the parameters are given in the plot. In figure 8 we can see, that downstream shock-impingement, a strong growth of all generated disturbance modes occurs. The highest amplitude is reached by $(0, 2)$, which represents the first directly generated streak-

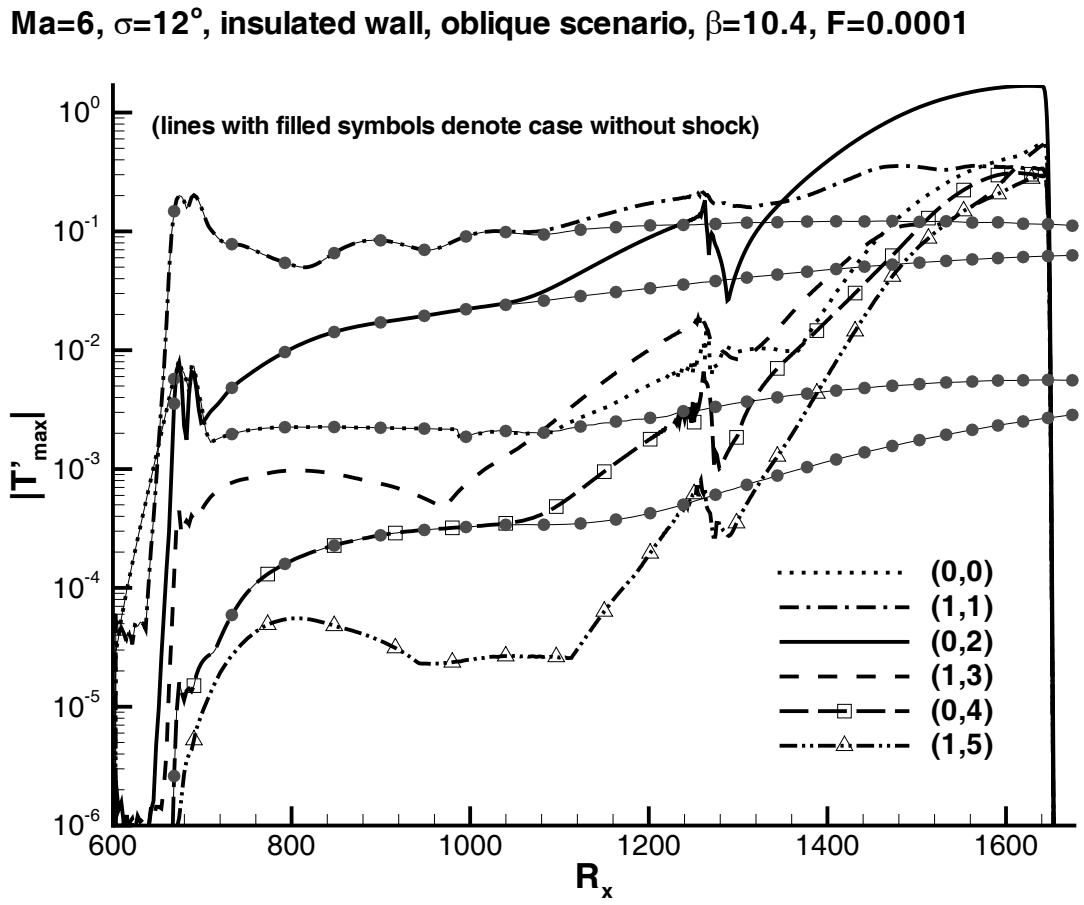


Figure 8. Maximum temperature disturbance amplitudes. Lines with symbols represent case without shock. $\sigma = 12^o$, insulated wall, oblique disturbance scenario. Spanwise wave number $\beta = 10.4$, disturbance frequency $F = 1 \cdot 10^{-4}$.

or vortex mode. Compared to the case without shock, the amplitudes of the disturbance modes in the case with shock exceed the corresponding amplitudes in the case without shock by several orders of magnitude.

Figure 9 shows maximum temperature amplitudes of the case with $T_w = 300K$. We observe a similar behaviour compared to the insulated case. However, maximum amplitudes reach smaller values in the case with $T_w = 300K$. In the case with $T_w = 300K$, the amplitude of $(0, 2)$ is increased by a factor of $\approx 47$ from the beginning of its rise, while in the insulated wall-case, this factor is $\approx 63$. It has to be noted that the initial amplitude of the disturbances is slightly smaller in $T_w = 300K$, compared to the adiabatic case.

Figure 10 shows the single vortex mode $(0, 2)$ for the adiabatic case at $R_x = 1600$, a location where it already reaches considerable amplitudes. The left picture shows the spanwise disturbance velocity field and selected streamlines. The right picture gives the wall-normal distributions of the disturbance velocity components $v'$ in wall-normal direction and $w'$ in spanwise direction. From the streamlines in the left picture of figure 10 we see four counter-rotating vortices with their cores at $y \approx 1.5$. If we add the largest vortex modes and the changes to the base-flow, which are represented by $(0, 0)$, to the base-flow, we again have four

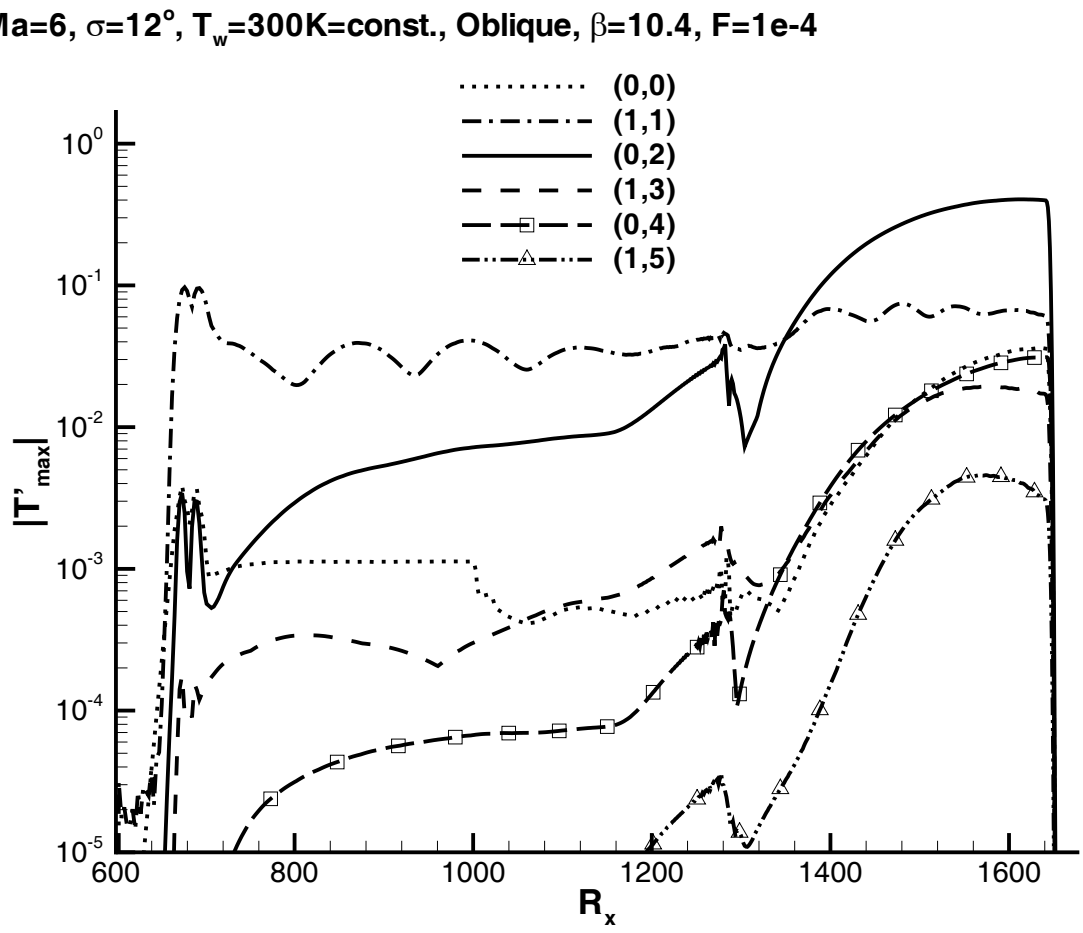


Figure 9. Maximum temperature disturbance amplitudes. $\sigma = 12^o$, $T_w = 300K$, oblique disturbance scenario. Spanwise wave number $\beta = 10.4$, disturbance frequency $F = 1 \cdot 10^{-4}$.

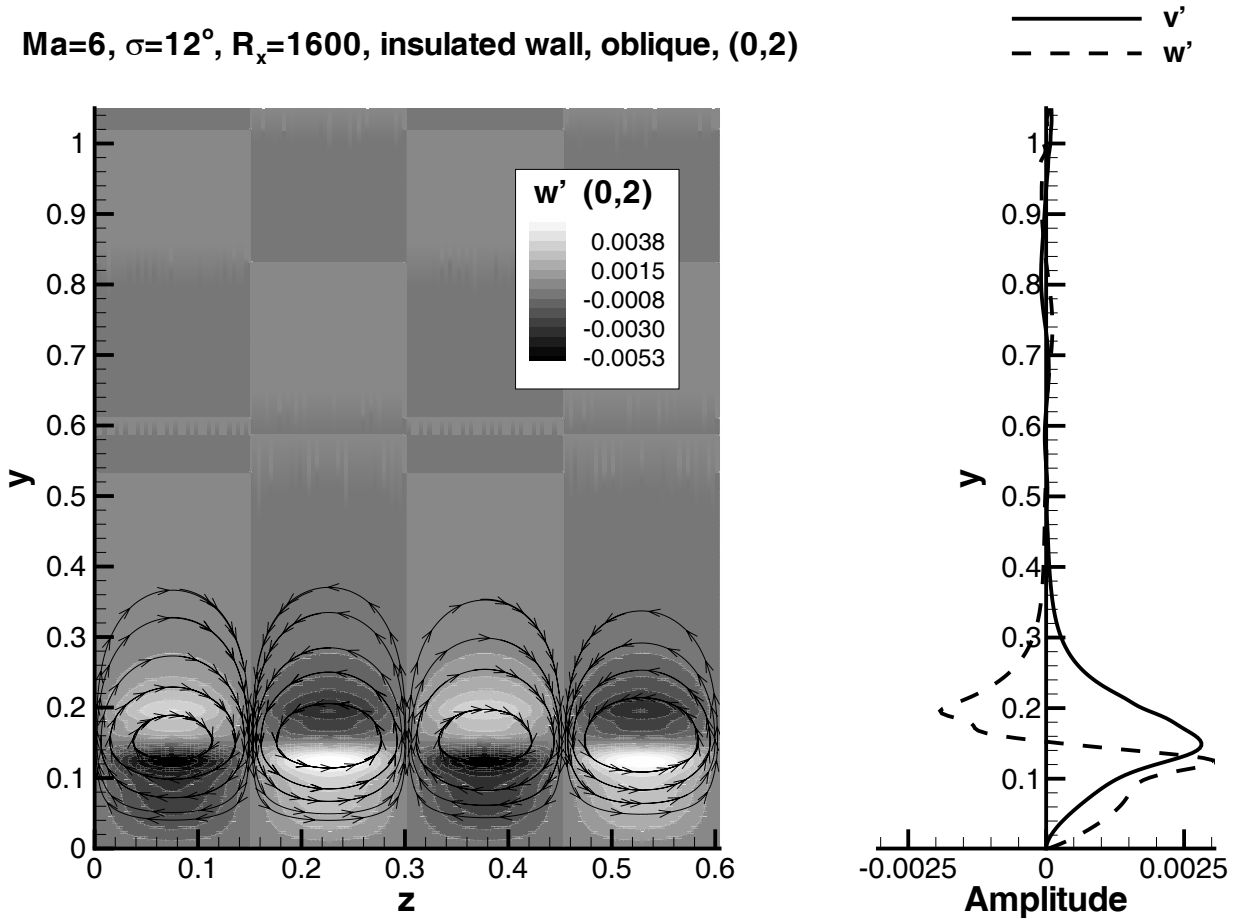


Figure 10. Spanwise disturbance velocity component (grey colour map) and selected streamlines are given in the left picture, while in the right picture, the wall-normal disturbance velocity distributions of $w'$ and $v'$ are shown. Single $(0,2)$-mode, $\sigma = 12^o$, $R_x = 1600$, insulated wall, oblique disturbance scenario. Spanwise wave number $\beta = 10.4$, disturbance frequency $F = 1 \cdot 10^{-4}$.

counter-rotating vortices, which can be seen in figure 11.

In the case without shock (figure 13), the single $(0,2)$-mode has a different shape. Instead of one single vortex in wall-normal direction, two vortices are present. As expected, the maximum values of the disturbance velocity components $v'$ and $w'$ are significantly smaller, compared to the case with shock. In the total flow, there are no vortices in the case without shock, which can be seen in figure 12.

Figure 14 gives an explanation for this. Wall normal base-flow velocity components are given for both the cases without impinging shock wave (left picture) and $\sigma = 12^o$. While in the case with shock, the magnitude of the $v$-component of the base flow is exceeded by the according disturbance velocity component around the vortex core, this is not the case without impinging shock wave. For both the upper and lower vortices in figure 13, the magnitude of the base flow is one order of magnitude higher than the disturbance amplitude $v'$. While the behaviour of the total flow in the case with $\sigma = 12^o$ is dominated by the $(0,2)$, in the case without shock it is still the base flow, which is dominating.

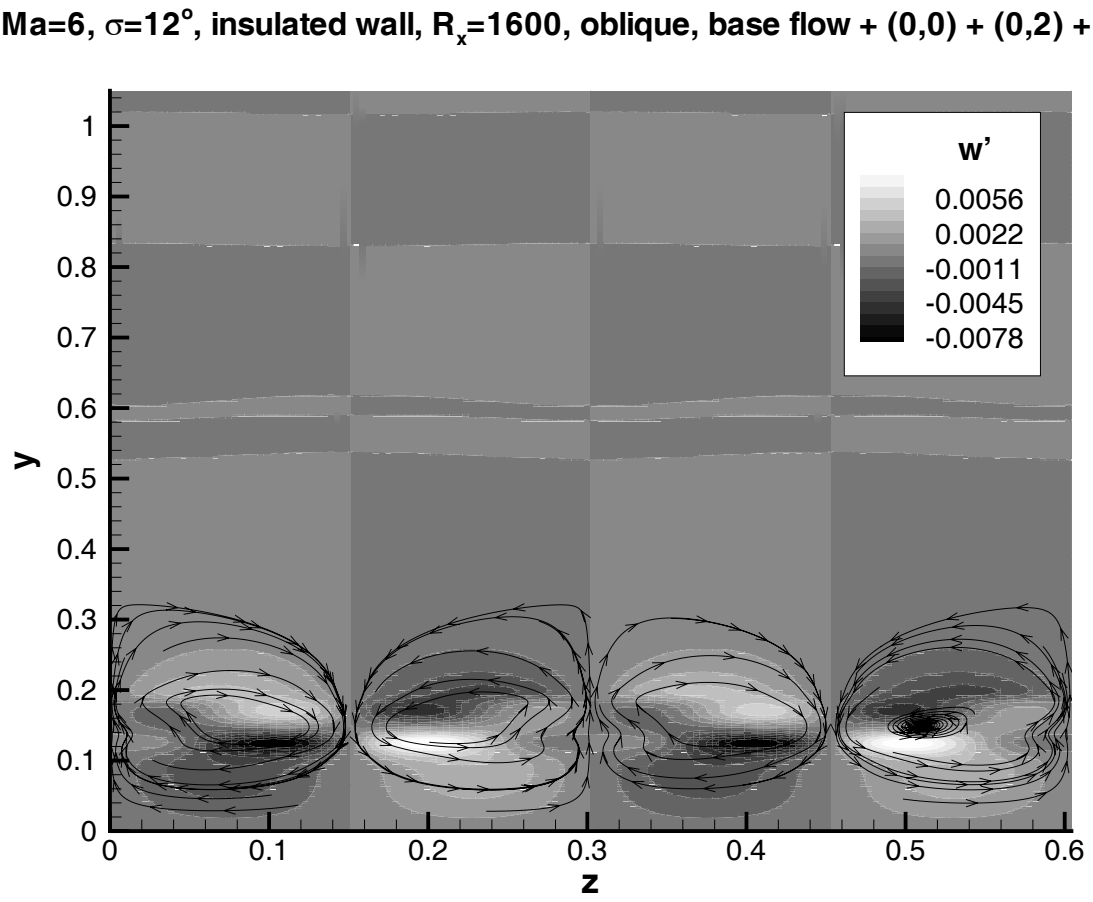


Figure 11. Spanwise disturbance velocity component (grey colour map) and selected streamlines of the total flow are given. $\sigma = 12^o$, $R_x = 1600$, insulated wall, oblique disturbance scenario. Spanwise wave number $\beta = 10.4$, disturbance frequency $F = 1 \cdot 10^{-4}$.

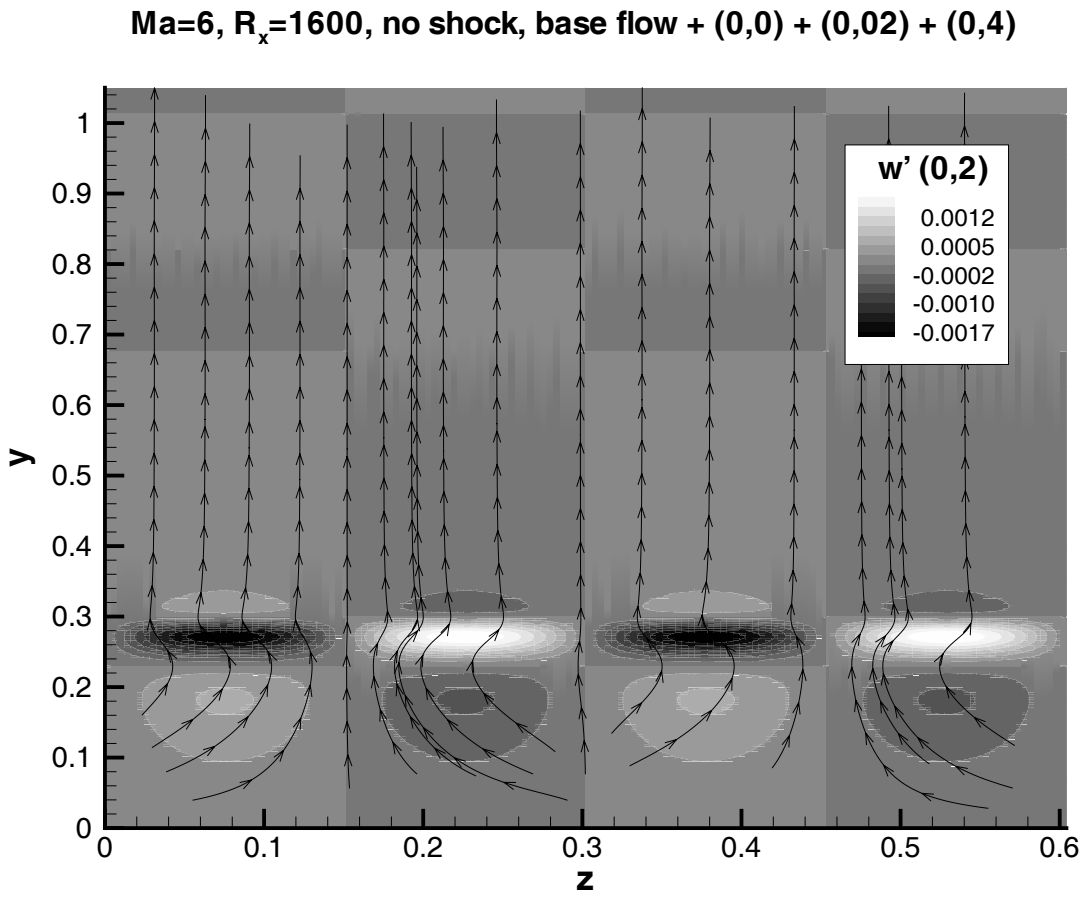


Figure 12. Spanwise disturbance velocity component (grey colour map) and selected streamlines of the total flow are given. No shock, $R_x = 1600$, insulated wall, oblique disturbance scenario. Spanwise wave number $\beta = 10.4$, disturbance frequency $F = 1 \cdot 10^{-4}$.

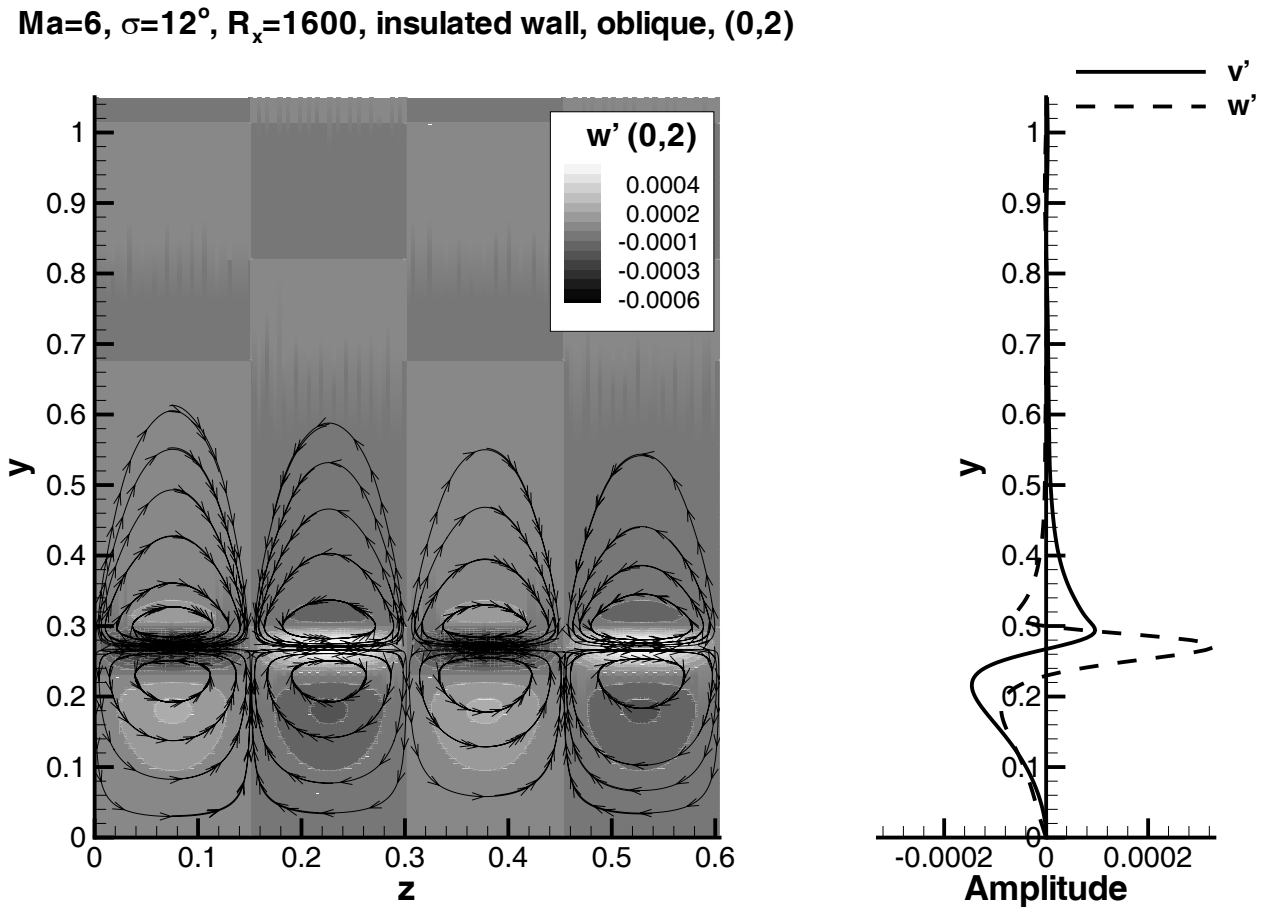


Figure 13. Spanwise disturbance velocity component (grey colour map) and selected streamlines are given in the left picture, while in the right picture, the wall-normal disturbance velocity distributions of $w'$ and $v'$ are shown. Single $(0,2)$-mode, no shock, $R_x = 1600$, insulated wall, oblique disturbance scenario. Spanwise wave number $\beta = 10.4$, disturbance frequency $F = 1 \cdot 10^{-4}$.

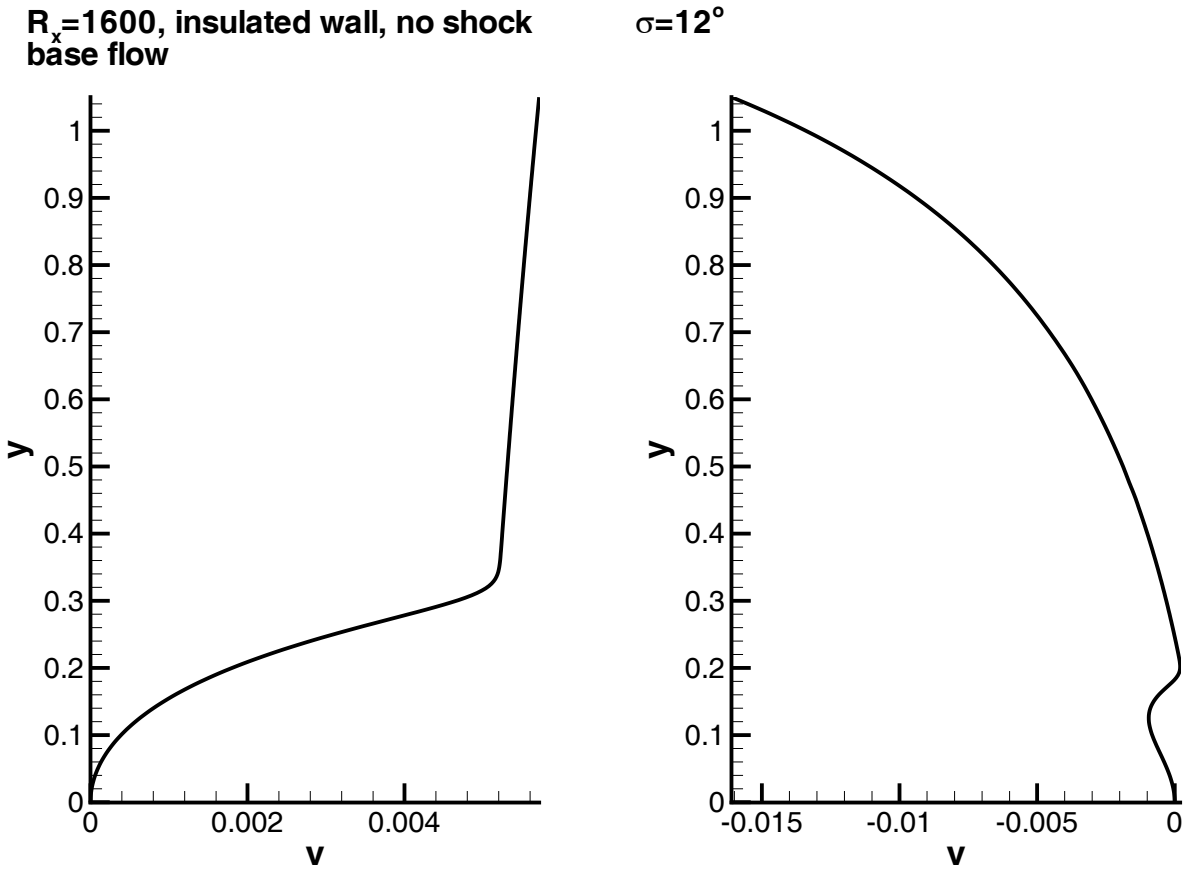


Figure 14. Wall-normal velocity distribution of the base flow at $R_x = 1600$ for the case without shock (left picture) and $\sigma = 12^o$.

# 5. Conclusion

Numerical simulations for a boundary layer at $Ma = 6$, $T_\infty = 78K$ with impinging shock wave (shock angle $\sigma = 12^o$) both for a constant wall-temperature of $T_w = 300K$ and insulated wall conditions have been presented. In the base flow, wall-cooling decreases the length of the separation bubble. In the underlying case, the length of the separation bubble could be decreased to 60% of the corresponding value with insulated wall. For small disturbance amplitudes, first mode instabilities have been completely stabilised with wall cooling. However, cooling caused a significant destabilisation of the second mode. In the investigations with larger disturbance amplitudes, in both cases vortices could be identified in the oblique breakdown scenario. In a similar case without shock-boundary layer interaction, vortices are not present, because of a different shape and smaller magnitude of the $(0, 2)$-mode and the $v$-component of the base flow velocity counteracting the formation of vortices in the case without shock. As in the linear case, the maximum disturbance amplitudes in the oblique scenario reach higher values for the insulated case.

# References

[1] In *CEAS TRA3 conference proceedings*, pages 33.1–33.13. Roy. Aer. Soc., 2002.

[2] J. Ackeret, F. Feldmann, and N. Rott. Untersuchungen an verdichtungsstößen in schnell bewegten gasen. Technical Report 10, ETH Zürich, Institut für Aerodynamik, 1946.

[3] J.D. Anderson Jr. *Computational Fluid Dynamics.* McGraw-Hill, international edition, 1995.

[4] D. Aymer de la Chevalerie, L. De Luca, and G. Cardone. Görtler-type vortices in hypersonic flows: The ramp problem. *Experimental Thermal and Fluid Science*, 15:69–81, 1997.

[5] C. Canuto, M.Y. Hussaini, A. Quarteroni, and T.A. Zang. *Spectral Methods in Fluid Dynamics.* Springer, 1987.

[6] L. De Luca and G. Cardone. Viscous interaction phenomena in hypersonic wedge flow. *AIAA Journal*, 33:2293–2298, 1995.

[7] J. Délery and J.G. Marvin. Shock-wave boundary layer interactions. *AGARDograph*, 280, 1986.

[8] Eißler, W., and H. Bestek. Spatial numerical simulations of linear and weakly nonlinear wave instabilities in supersonic boundary layers. *Theoret. Comput. Fluid Dynamics*, 8:219–235, 1996.

[9] W. Eißler. *Numerische Untersuchungen zum laminar-turbulenten Strömungsumschlag in Überschallgrenzschichten.* PhD thesis, Universität Stuttgart, 1995.

[10] A. Fedorov, A. Shiplyuk, A. Maslov, E. Burov, and N. Malmuth. Stabilization of a hypersonic boundary layer using an ultrasonically absorptive coating. *J. Fluid Mech.*, 479:99–124, 2003.

[11] A. Fezer and M. Kloker. Transition process in Mach 6.8 boundary layers at varying temperature conditions investigated by spatial direct numerical simulation. In W. Nitsche, H. J. Heinemann, and R. Hilbig, editors, *New Results in Numerical and Experimental Fluid Mechanics II*, volume 72 of *Notes on Numerical Fluid Mechanics*, pages 138–145. Vieweg, 1999.

[12] P. Harris. *Numerical investigation of transitional compressible plane wakes.* PhD thesis, University of Arizona, 1993.

[13] C. Hirsch. *Numerical Computation of Internal and External Flows, Volume 1.* John Wiley and Sons, 1988.

[14] M. Kloker, U. Konzelmann, and H. Fasel. Outflow boundary conditions for spatial Navier-Stokes simulations of transition boundary layers. *AIAA J.*, 31:620–628, 1993.

[15] M.J. Kloker. A robust high-resolution split-type compact FD scheme for spatial direct numerical simulation of boundary-layer transition. *Applied Scientific Research*, 59:353–377, 1998.

[16] A.D. Kosinov, A.A. Maslov, and S.G. Shevelkov. Experiments on the stability of supersonic boundary layers. *J. Fluid Mech.*, 219:621–633, 1990.

[17] S.K. Lele. Compact finite difference schemes with spectral-like resolution. *J. Comp. Phys.*, 103:16–42, 1992.

[18] H.W. Liepmann. The interaction between boundary layer and shock waves in transsonic flow. *J. Aeronaut. Sci.*, 13:623–637, 1946.

[19] L.M. Mack. Boundary layer stability theory. Technical Report 900-277, Jet Propulsion Laboratory, Pasadena, 1969.

[20] A. Pagella, U. Rist, and S. Wagner. Numerical investigations of small-amplitude disturbances in a boundary layer with impinging shock wave at Ma=4.8. *Phys. Fluids*, 14 (7):2088–2101, 2002.

[21] W.H. Press, S.A. Teukolsky, W.T. Vetterling, and B.P. Flannery. *Numerical Recipes in Fortran.* Cambridge University Press, second edition edition, 1992.

[22] K.W. Thompson. Time dependent boundary conditions for hyperbolic systems. *J. Comput. Phys.*, 68:1–24, 1987.

[23] A. Thumm. *Numerische Untersuchungen zum laminar-turbulenten Strömungsumschlag in transsonischen Grenzschichtströmungen.* PhD thesis, Universität Stuttgart, 1991.